Journal of Power Sources 189 (2009) 935–942

Contents lists available at ScienceDirect

Journal of Power Sources

journal homepage: www.elsevier.com/locate/jpowsour

Assessing the catalyst processing for low temperature cofired ceramic-based direct methanol fuel cells

Yong Gao, Norman Munroe*, Xiangxing Kong, Kinzy Jones

Department of Mechanical and Materials Engineering, Florida International University, Miami, FL 33174, USA

ARTICLE INFO

Article history:
Received 11 November 2008
Received in revised form 18 December 2008
Accepted 19 December 2008
Available online 8 January 2009

Keywords:
Catalyst processing
Catalyst evaluation
Low temperature cofired ceramic (LTCC)
Micro-direct methanol fuel cells
(micro-DMFCs)

ABSTRACT

The low temperature cofired ceramic (LTCC) process has emerged as a promising technique to produce miniature direct methanol fuel cells (DMFCs). The currently manufactured LTCC-based DMFCs are mechanically assembled from separate components and do not take advantage of the integration merits. In order to reduce the number of stages for the production of LTCC-based DMFCs, two catalyst-loading procedures were investigated: postfiring and cofiring on the porous Ag electrodes. The performance of the catalyst on electrodes prepared by both methods was evaluated by XRD, TEM and cyclic voltammetry (CV). The postfired (PF) anode catalyst had a particle size of 5.6 nm as calculated by XRD, which was consistent with the TEM observation of 4.8 nm. XRD analysis confirmed the formation of a Pt–Ru alloy, but to a lesser extent in PF anode catalyst. The cofired (CF) anode catalyst revealed the presence of precipitated whiskers within the pores that consisted mainly of Ag and Pt–Ru alloy with a very small amount of Ru. The PF cathode catalyst film consisted of Ag and a small amount of Pt–Ag alloy, with some pore blockage by the catalyst film. The CF cathode catalyst displayed two morphologies: particles comprised of Pt precipitate and agglomerated particles comprised of Ag–Pt alloy. The electrochemical evaluation revealed that methanol oxidation reaction (MOR) on the CF catalyst anode outperformed the PF catalyst anode. This was attributed to the larger surface area, uniform catalyst composition, higher degree of alloying and ternary catalyst effects. The CF cathode catalyst also indicated superior oxygen reduction reaction (ORR) performance in terms of current density as compared with that of the PF catalyst. The experimental analysis indicated that the CF catalyst-loading method is superior to the PF for LTCC-based DMFC fabrication.

1. Introduction

The miniature direct methanol fuel cell (DMFC) has been envisaged as a suitable power source for portable devices due to its simplicity, compactness, light weight, high power density, and ease of delivery and storage of its liquid fuel [1].

Currently, miniature silicon-based DMFCs or micro-DMFCs are fabricated by microelectromechanical systems (MEMS) technique, which requires complex processing and the use of high precision and expensive equipment. The Si-based miniature DMFC faces the challenges of structurally assembling and sealing Si, which is brittle, low conductivity of the electrode, and relatively high large scale manufacturing cost. Many other techniques have been attempted to prepare miniature DMFCs, such as low temperature cofired ceramics (LTCC) [2], photochemical etching of thin stainless steel plates for electrodes [3] and sputtering method on either side of a microporous plastic substrate [4].

LTCC allows the integration of numerous components, including embedded passives, high density interconnects and a layered construction with embedded micro-channels within the multilayers. The LTCC product is superior to those from other processes principally due to its high thermal and chemical stability, ease of fabrication, high mechanical strength, low material cost and hermetic sealing of the structure [5]. The LTCC-based DMFCs demonstrated by Motorola Lab [2] still are comprised of separate components, a design which does not take advantage of the above-mentioned features. In our LTCC-based DMFC design, an embedded porous silver tape replaces the traditional carbon electrode to overcome its deficiencies such as brittleness, lower conductivity and poor machinability [6]. Ag is widely used in LTCC fabrication for conductive metallization [7,8] and thus can be cofired in situ. A silver thick film tape embedded into a LTCC structure for thermal management application has been successfully developed [9], and a similar technique was adopted to manufacture a porous Ag tape in this work.

A critical issue affecting DMFC's performance is the need of a high performance catalyst. Numerous attempts have been made to prepare catalysts on carbon electrodes by employing techniques

* Corresponding author. Tel.: +1 305 348 3556; fax: +1 305 348 1852.
E-mail address: munroen@fiu.edu (N. Munroe).

0378-7753/$ – see front matter © 2008 Elsevier B.V. All rights reserved.
doi:10.1016/j.jpowsour.2008.12.119

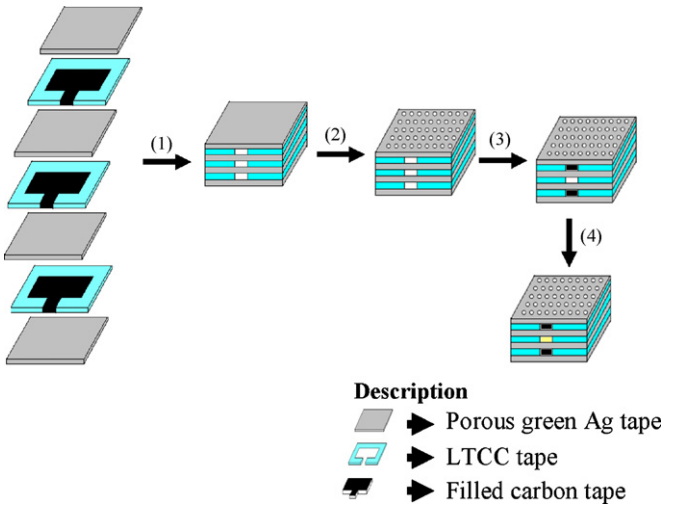

Fig. 1. Schematic processing of postfired LTCC-base DMFC structure.

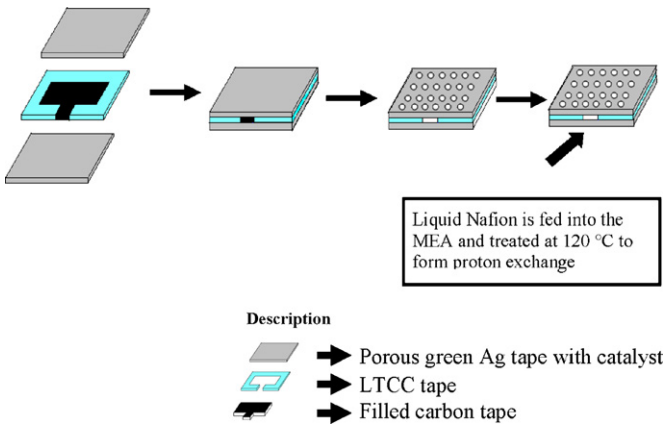

Fig. 2. Schematic processing of cofired LTCC-base DMFC structure.

such as impregnation [10–12], colloidal precipitation [13,14], microemulsion [15,16], and coprecipitation [17,18]. These chemical methods generally utilize toxic, combustible or explosive reductants, and involve several stages for filtration, washing, centrifuging and vacuum drying under hydrogen. As a result, the reactions are difficult to control and the process is expensive. This is not the case with LTCC, where the catalyst is prepared by pyrolysis, which greatly decreases the factors that affect the catalyst performance. Two LTCC-based processing methods are proposed for manufacturing miniature DMFC catalyst structure: postfiring (PF) and cofiring (CF). Fig. 1 is a schematic illustration of the PF DMFC process. The detailed steps are as follow: (1) A porous Ag tape is prepared for the electrode. Then a LTCC tape frames a cavity that is filled with carbon tape, which serves as a sacrificial phase. The assembly is then laminated together; (2) the structure is fired according to the following temperature regimes: heat to 450 °C for 2 h to remove the organic phase, then heat to 650 °C for 2 h to remove the carbon tape, followed by heating to 850 °C for 15 min and cooling naturally; (3) after firing, a LTCC structure with three cavities and four layers of porous Ag tape is formed. The top and bottom porous Ag tapes serve as the diffusion layers and the middle two thin porous Ag tapes serve as the anode and cathode, respectively. In order to facilitate the three phase interface, the catalyst ink is gravity fed into the upper and lower cavities prior to heat treatment to produce the catalyst layers (black color in cavity); (4) finally a solution of liquid Nafion™ and PTFE (20–30 wt%) are introduced into the cavity followed by heat treatment at 120 °C for 15 min to produce the PEM membrane. A schematic process for producing CF LTCC-based DMFC structure is presented in Fig. 2. In this process, the catalyst ink is directly added into the Ag tape raw materials prior to the tape casting process. The tape is then laminated with the cavity frame (LTCC tape). Obviously, the cofired process is simpler and results in a simple structure.

In this work, the pyrolyzed resinate-based catalyst produced by the PF and CF LTCC processes were evaluated in an effort to determine the better process to manufacture LTCC-based DMFCs.

2. Experimental

2.1. Porous Ag electrode and catalyst preparation

The porous Ag electrode was prepared by mixing 3 g of Ag powder (PM225, Hereaus, PA) with 0.6 g graphite (pore forming agent, Aldrich), 9 mg polyacrylic acid (dispersant, Hereaus, PA), 7.1 mg dipropolene glycol dibenzoate (plasticizer, Hereaus, PA), and 0.19 g Paraloid B-72 (binder, Hereaus, PA) in methyl ethyl ketone solvent (Fisher, NJ). The mixture was stirred to produce a viscous slurry before it was casted on mylar. After drying, it was peeled off forming the Ag tape.

The porous Ag tape was fired with the previously described temperature regime for the LTCC. The PF anode catalyst was prepared by mixing platinum resinate and ruthenium resinate (BASF, CA) in a molar ratio of 1:1. The mixture was then brushed on the fired porous Ag tape surface and heated at 500 °C with a ramp rate of 2 °C min^{-1} in air for 4 h. In the case of the PF cathode catalyst, only platinum resinate was used with heating at 380 °C.

The CF anode catalyst was prepared by mixing the catalyst ink with platinum and ruthenium resinates (64 mg catalyst ink and 1:1 molar ratio Pt–Ru) which were added to porous Ag tape. The mixture was then fired as previously described.

2.2. Physical characterization

The X-ray diffraction (XRD) analysis was conducted on PF and CF electrodes using a Siemens Diffraktometer D500 with Cu Kα source (λ = 1.542 Å) operated at 40 keV and 20 mA with a scan rate of 0.1° S^{-1} with 2θ sweep from 15° to 90°. A scanning electron microscope (JEOL JSM-633OF) was used to examine the morphology of the electrodes. The atomic composition was analyzed by an energy dispersive X-ray (EDX) spectrometer, which was integrated with the SEM instrument. Samples of the electrode were ultrasonically dispersed in ethanol before being placed on the carbon-coated grid for analysis by Transmission Electron Microscope (TEM, Philips CM 200).

2.3. Electrochemical measurement

Cyclic voltammetry (CV) was performed on electrodes using a Solartron 1287/1260 impedance system with Pt as the counter electrode and a saturated calomel electrode (SCE) as the reference electrode. All potentials were quoted with respect to the reference SCE electrode.

The CVs of methanol oxidation reaction (MOR) on the anode catalyst (working electrode) were measured using 0.5 M H_2SO_4 solution in 1.0 M CH_3OH at a scan rate of 20 mV s^{-1} over the potential range −0.2–0.6 V (vs. SCE). Prior to each electrochemical measurement, oxygen was purged from the solution by bubbling high-purity nitrogen for 30 min. The CVs of oxygen reduction reaction (ORR) on the cathode catalyst were measured in 0.5 M H_2SO_4 solution with a sweep rate of 20 mV s^{-1} after purging with high purity nitrogen for 30 min. The scanning potential range was the same as with the anode. All measurements were carried out at 60 °C.

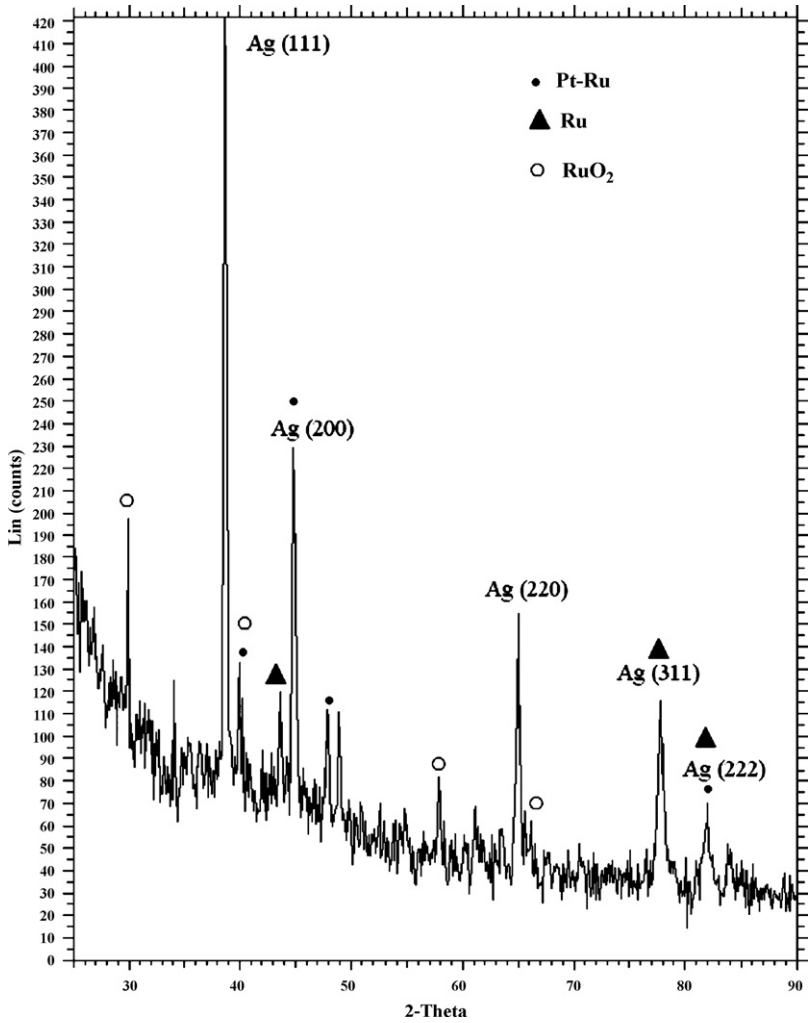

Fig. 3. XRD of 1:1 Pt resinate and Ru resinate mixture heated at 500 °C in air for 4 h.

3. Results and discussion

3.1. Anode physical characterization

The morphology and physical characteristics of the PF and CF anode electrodes were investigated using XRD, SEM and TEM.

3.1.1. Postfired anode catalyst characterization

The standard diffraction peaks of each element or compound detected in this investigation are listed in Table 1, from which the average particle size of the catalyst was determined. The XRD pattern of the PF anode sample (Fig. 3) exhibited peaks of Ag (1 1 1), Ag (2 2 0) and Ag (3 1 1) that were slightly shifted to higher 2θ values. This implied the formation of Ag alloys [19]. In addition, the peak at 81.97° indicated the formation of a small amount of Ag–Pt alloy since the peak shifted to a litter higher 2θ value as compared with the standard Ag peak. The diffraction peaks at 44° Ru (1 0 1) and 78° Ru (1 0 3) corresponding to the HCP structure of Ru were also observed. The peaks at 28°, 35° and 58° were associated with the formation of RuO_2.

The average particle size of the catalyst heat treated at 500 °C was calculated from broadening of the (2 2 0) diffraction peak using Scherrer's equation [20]:

$$d = \frac{0.9\lambda}{B_{2\theta}\cos\theta_{\max}} \quad (1)$$

where λ is the wavelength of the X-ray (1.54056 Å), θ is the angle at the maximum of the peak and $B_{2\theta}$ is the width of the peak at half height. An average particle size of 5.6 nm was calculated from the XRD peak widths, which was similar to that obtained by TEM

Table 1
The Standard XRD peaks of related elements and compound.

Elements or compound			
Pt (JCPDS Card # 04-0802)		Ag (JCPDS Card # 04-0783)	
(*h k l*)	2θ	(*h k l*)	2θ
1 1 1	39.9	1 1 1	38.12
2 0 0	46.7	2 0 0	44.29
2 2 0	67.7	2 2 0	64.45
3 1 1	81	3 1 1	77.47
		2 2 2	81.54
Elements or compound			
Ru (JCPDS Card # 06-0663)		RuO_2 (JCPDS Card # 21-1172)	
(*h k l*)	2θ	(*h k l*)	2θ
1 0 0	38.4	1 1 0	28.01
0 0 2	42.15	1 0 1	35.05
1 0 2	58.4	2 0 0	40.02
1 1 0	69.7	1 1 1	40.55
1 0 3	78	2 1 1	54.25
2 0 0	82	2 2 0	57.93
		0 0 2	59.4

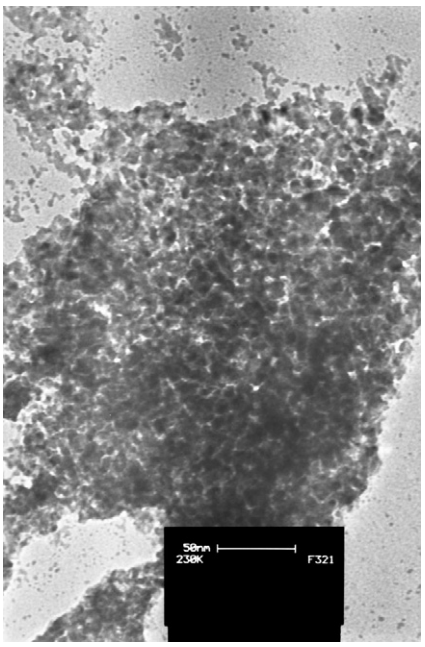

Fig. 4. The TEM of PF Pt–Ru catalyst.

(4.8 nm, Fig. 4).

$$a_{\mathrm{fcc}} = \frac{\sqrt{2}\lambda_{K\alpha 1}}{\sin\theta_{\max}} \quad (2)$$

A Pt lattice parameter, a_{fcc} of 3.894 Å using the Pt (2 2 0) diffraction peak was calculated from Eq. (2) and found to be less than that of pure Pt, 3.923 Å. This contraction of the Pt lattice parameter was attributed to the formation of the FCC Pt–Ru alloy [21].

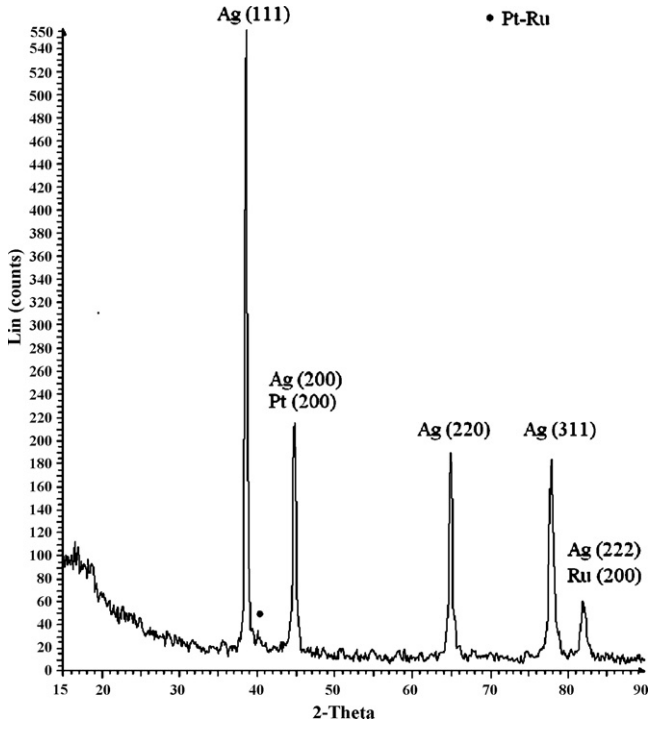

Fig. 5. XRD pattern of CF anode catalyst followed LTCC firing schedule.

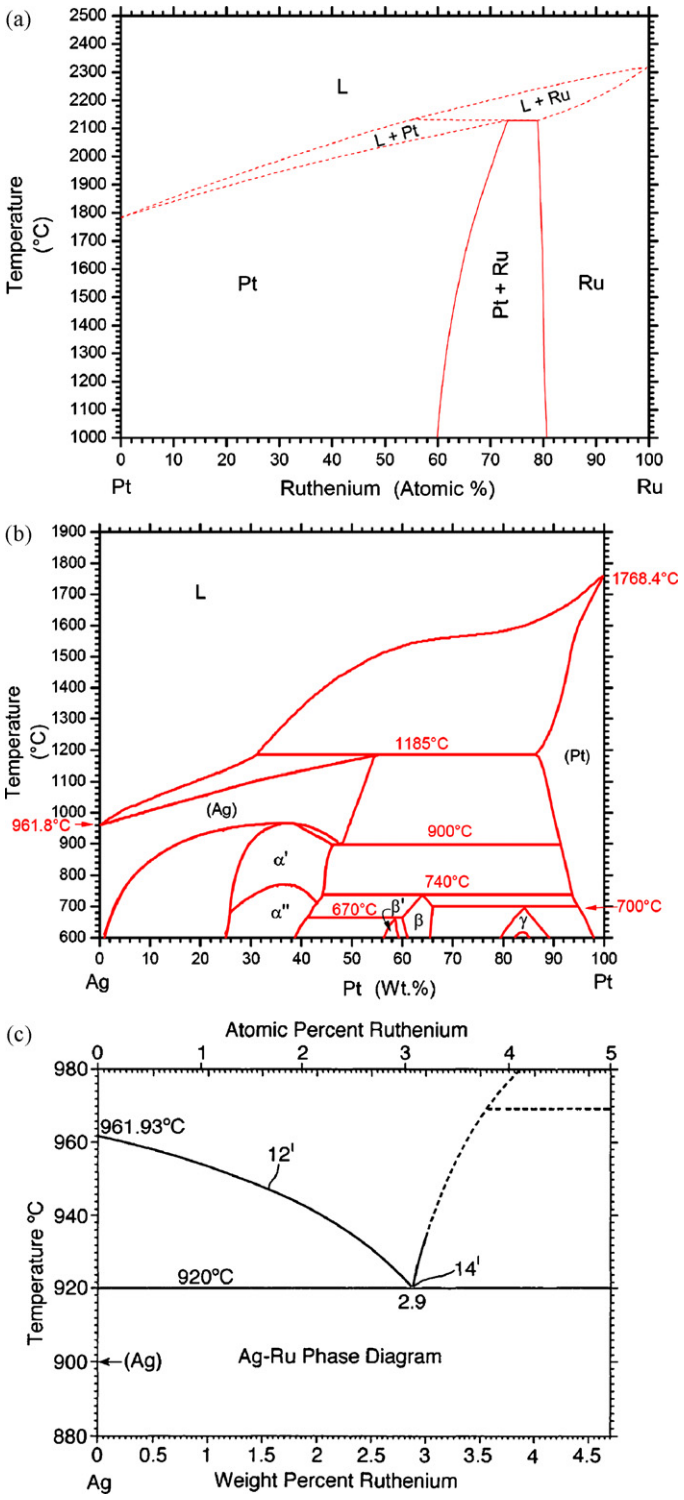

Fig. 6. Pt–Ru (a), Ag–Pt (b) and Ag–Ru (c) binary alloy phase diagram [22].

The atom fraction of Ru in the Pt–Ru alloy catalyst was determined using the following equation [11,22]:

$$a_{\mathrm{fcc}} = l_{\mathrm{oc}} - kX_{\mathrm{Ru}} \quad (3)$$

where l_{oc} = 3.9155 Å (the lattice parameter for pure Pt) and k = 0.124 Å is a constant. A Ru atom fraction of 0.17 implied that only a small amount of Ru was alloyed whilst the bulk of it remained in the amorphous state.

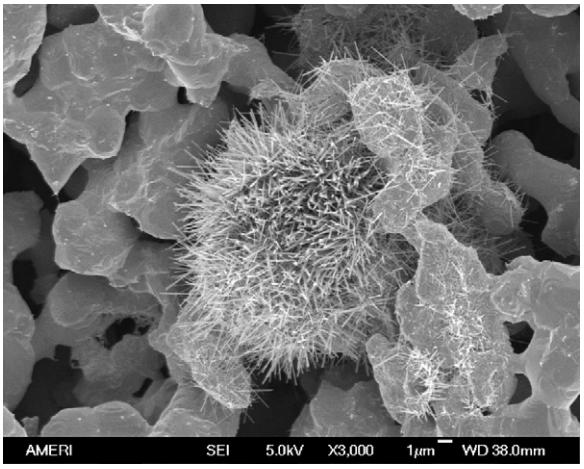

Fig. 7. The microstructure of CF porous Ag tape with catalyst.

3.1.2. *Cofired anode catalyst characterization*

Fig. 5 shows the XRD pattern of the CF electrode catalyst (which involves the three elements Pt, Ag and Ru), that was fired at 850 °C. The Pt–Ru, Ag–Pt and Ag–Ru binary phase diagrams (Fig. 6) [22] reveal that Pt–Ru and Pt–Ag are solid solutions and Ag and Ru are immiscible at 850 °C. However, no conclusion could be drawn on whether any other solid solution phase exists since a Ag–Pt–Ru ternary phase diagram is not available.

The strongest peak identified in the XRD analysis corresponded to Ag, which comprised the bulk of the porous Ag tape. No diffraction peaks corresponding to pure platinum phase was obtained, which indicated that both a noble metal oxide and alloy were produced after sintering. It should be noted that the ratio of the Pt and RuO_2 diffraction peak intensities in the XRD analysis (Fig. 5) was proportional to the contents of Pt and Ru in the tape. The XRD data (not shown here) of Pt–Ru resinate heated on Al_2O_3 substrate at different temperatures (370, 500, 600, 700 and 850 °C) revealed that the degree of alloying increased with temperature. This confirmed that the CF process resulted in greater alloy formation as compared with the PF process. Furthermore, the relatively narrow Pt–Ru XRD peaks of the CF catalyst indicated a high degree of crystallinity in the alloy produced after sintering [23].

The microstructure of the CF anode catalyst is shown in Fig. 7, where a large amount of whiskers were formed within the pore structure. EDX analysis of the whiskers revealed a composition of 93.25 at.% Ag, 2.77 at.% Ru, and 3.98 at.% Pt atoms. So it was inferred that the whiskers were comprised mainly of Ag–Pt and Pt–Ru solid solutions with a small amount of precipitated Ru. The average diameter of the whisker was approximately 50 nm with a length of about 1.2 μm. EDX analysis of the solid electrode surface revealed a composition of 87.84 at.% Ag, 6.62 at.% Pt, 3.32 at.% O and 0.14 at.% Ru which indicated that more Ru reported to the whisker.

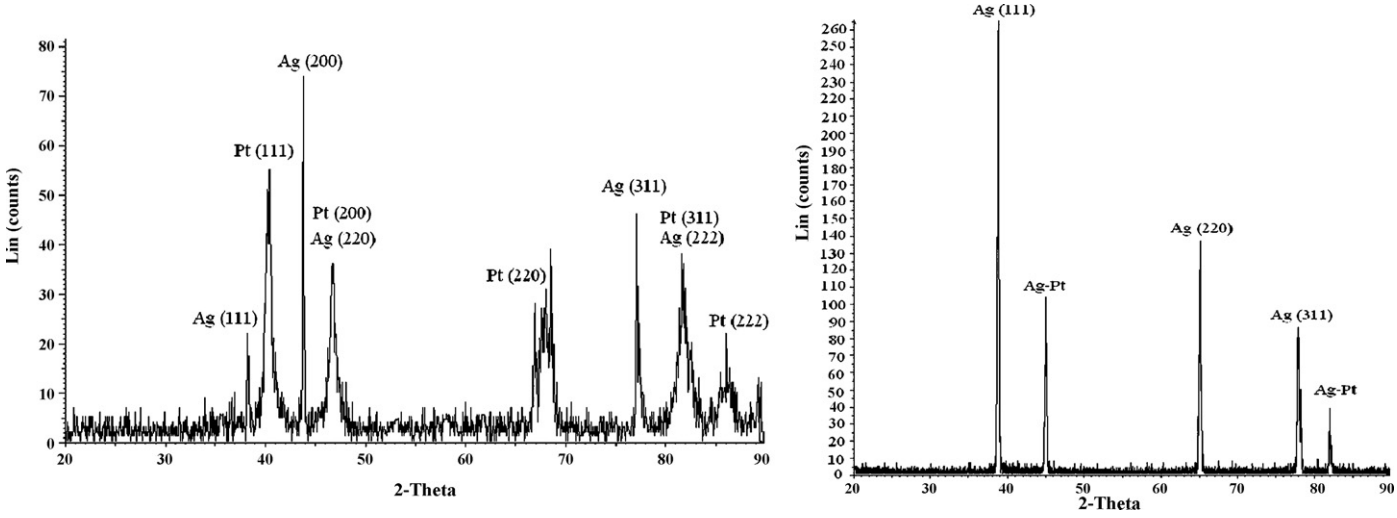

Fig. 8. XRD pattern of Cathode catalyst of PF (left) and CF (right).

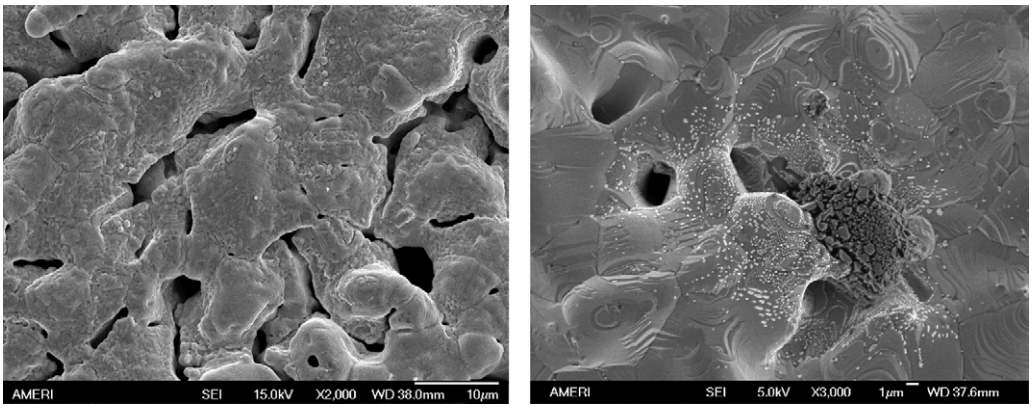

Fig. 9. Microstructure of postfired cathode catalyst on porous Ag surface (left) and cofired cathode catalyst (right).

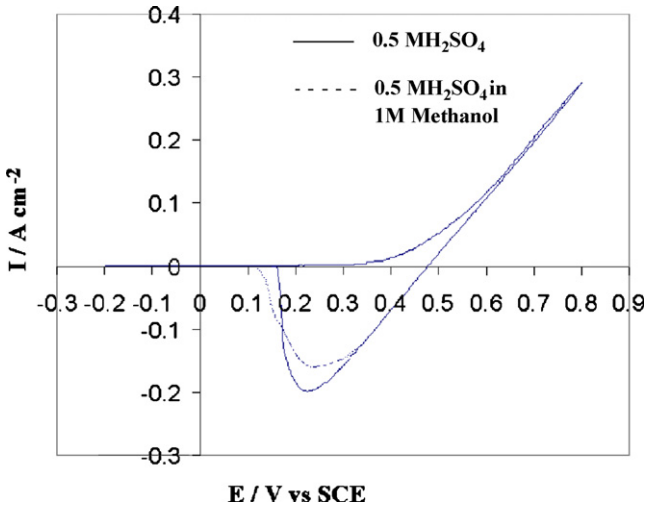

Fig. 10. CV of porous Ag tape in 0.5 M H_2SO_4 at 60 °C with sweep rate of 20 mV s^{-1}.

3.2. Cathode physical characterization

Fig. 8 shows the XRD pattern of the cathode catalyst under PF and CF conditions. Typical Pt and Ag peaks were observed with the PF catalyst. However, for the CF catalyst the 2θ peaks at 38.71°, 44.85°, 64.9°, 77.84° and 81.97° corresponded to the Ag–Pt alloy, which could not have been for silver, which has 2θ values at 38.12° (1 1 1), 44.29° (2 0 0), 64.45° (2 2 0), 77.47° (3 1 1), 81.54° (2 2 2). This indicated the incorporation of Pt into the Ag unit cell. The microstructures of the PF and CF cathode catalysts are presented in Fig. 9. The PF process resulted in a porous Ag surface, whereas the CF process resulted in a bi-modal morphology: small individual particles and agglomerated particles. Both morphologies consisted of Ag, Pt and O atoms. The white particles had a composition of 3.66 at.% Pt, 12.51 at.% O and 83.81 at.% Ag and the agglomerated particles had a composition of 82.79 at.% Ag, 4.34 at.% Pt and 12.88 at.% O. The Pt/Ag ratio in particles was lower than that in agglomerated particles. It was inferred that Pt and PtO_2 precipitated out of the Ag lattice structure in the case of the individual particles, whereas the agglomerated particles comprised of Ag and Pt–Ag solid solution.

3.3. Methanol oxidation reaction for anode catalyst

Since silver can react with sulfuric acid under DMFC operating conditions, the onset potential for this reaction was firstly determined. The cyclic voltamograms of the porous Ag tape in 0.5 M H_2SO_4 and 0.5 M H_2SO_4 in 1 M methanol at 60 °C are illustrated in Fig. 10, where it can be seen that the onset potential for the oxidation of the porous silver tape was 0.47 V_{SCE}. This onset potential was consistent with results published in the literature [24] as well as what was previously obtained using Ag wire.

In an effort to determine the onset potential for MOR under similar conditions, a carbon electrode with the same catalyst was utilized. In cyclic voltamogram of Fig. 11 indicated an onset potential of 0.34 V_{SCE} MOR on carbon. The cyclic voltamograms of PF and CF catalyst loaded porous silver tapes shown in Fig. 12 revealed an onset MOR potential of approximately 0.45 V_{SCE}.

It was revealed that MOR on Pt–Ru occurred over the range of 0.34–0.7 V_{SCE} (Fig. 11). Therefore, the voltage after 0.47 V_{SCE} in Fig. 12 is a combination of the onset potential for Ag oxidation and MOR on Pt–Ru catalyst. Subsequently, it is difficult to distinguish the contribution of each process after 0.47 V_{SCE}, and the voltage before 0.47 V_{SCE} was definitely due to the catalytic effect on MOR as depicted in Fig. 12. It can be concluded that the catalytic effect of the CF electrode on the MOR was superior to that of the PF, which

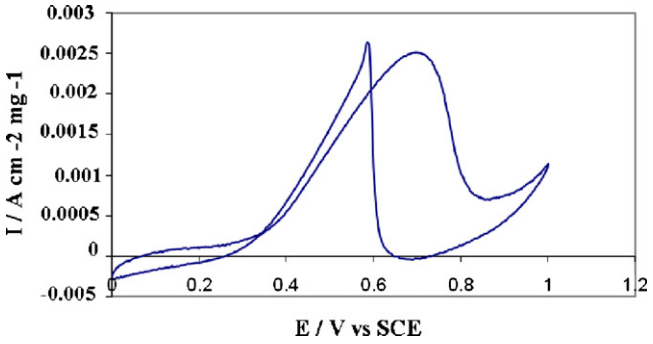

Fig. 11. CV of catalyst on carbon at 60 °C with a sweep rate of 20 mV s^{-1}.

may be attributed to high surface area of precipitated whiskers (Fig. 7), a highly alloyed ternary catalytic phase of relatively uniform composition (the primary catalytic phases being the Pt–Ru and the Pt–Ag).

It should be noted that the order of catalytic activity of Pt-based binary alloy catalysts is Pt–Ru > Pt–Os > Pt–Ag > Pt–Rh [25,26]. Furthermore, it has been reported [27] that Pt–Ru–Ag improves CO tolerance. Many studies [28–31] have been conducted on the electrooxidation of methanol using ternary catalysts (Pt–Ru–X, with X = Au, Co, Cu, Fe, Mo, Ni, Sn, W, P, or Rh). However, ruthenium and the ternary metal are considered primary elements responsible for active sites for the formation of oxy-species at low potentials, mainly through –OH groups [32]. The ternary element must be able to split the water molecule. Moreover, the catalyst needs to be stable in a highly acidic medium, which is necessary for the DMFC operation. The molecular orbital theory calculation predicts that the second transition element, such as Zr, Mo, Pd, and Ag has sufficiently high activity to cause OH bond scissions comparable to that of Ru [33].

It is also worth noting that the small current density peak corresponding to MOR on RuO_2 from 0.23 to 0.32 V_{SCE} in CF curve (Fig. 12) was obscured by the large current density peak. The CV plot in Fig. 13 of the CF sample scanned up to 0.35 V_{SCE} confirmed the current density peak for MOR on RuO_2.

3.4. Oxygen reduction reaction of cathode catalyst

A comparison of the catalytic ORR on PF and CF electrodes in 0.5 M H_2SO_4 at 60 °C is shown in Fig. 14. Actually, the peak in the range from 0.1 to 0.28 V_{SCE} is not evident in Fig. 14 due to the high current density after 0.5 V_{SCE}. A polarization plot to a potential of 0.4 V_{SCE} indicated this peak as shown in Fig. 15. Another ORR peak of Pt occurred in the range of 0.5–0.71 V_{SCE} [33,34]. Therefore, after

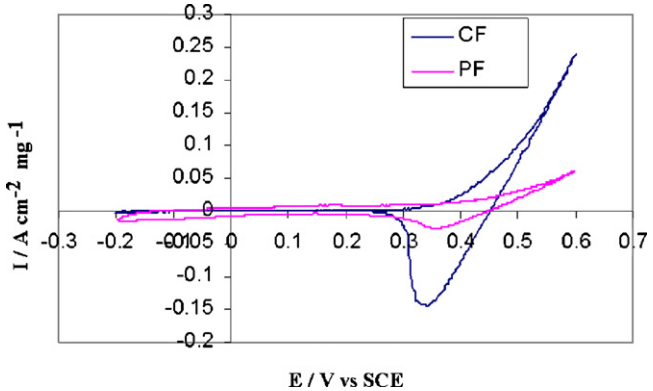

Fig. 12. The CV of PF and CF catalyst (in the solution of 0.5 M H_2SO_4 in 1 M CH_3OH) at 60 °C with a sweep rate of 20 mV s^{-1}.

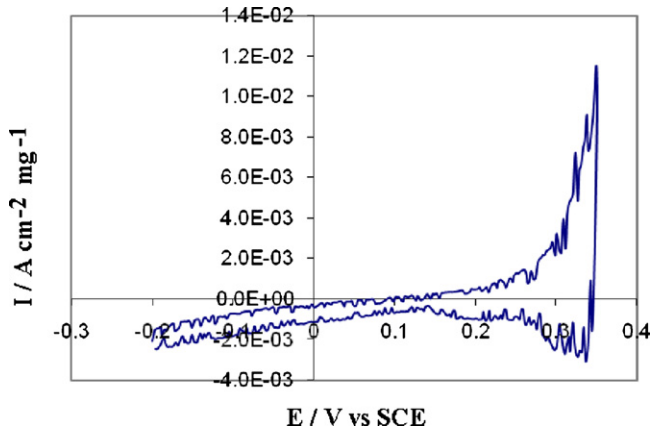

Fig. 13. The CV of CF sample up to 0.35 V (vs. SCE) at 60 °C with sweep rate 20 mV s^{-1}.

0.47 V_{SCE} there were three sources of ORR, i.e. ORR from Pt, Ag and Pt–Ag alloy (Note: the onset potential of porous Ag oxidation in 0.5 M H_2SO_4 was 0.47 V_{SCE}). Also, the ORR from Pt is dominant up to 0.47 V_{SCE}. The CV curves shown in Fig. 14 revealed that the ORR on the CF electrode was superior to that on PF in terms of current density. This was attributed to the presence of Pt and Pt–Ag alloy on the CF electrode. The combinatorial catalytic effect contributed to better ORR performance, which can be explained by an electronic factor, i.e. the change of the d-band vacancy in Pt upon alloying and/or by geometric effects (Pt-coordination number and Pt–Pt distance.) [35] Other contributing factors include a reduction of the Pt oxidation state [36] and suppression of Pt oxide formation [37].

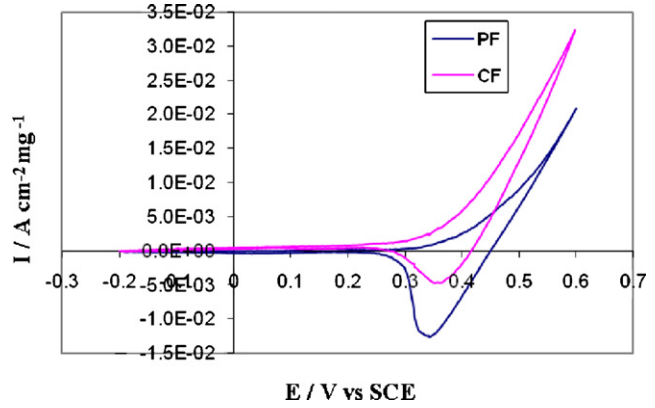

Fig. 14. CV of PF and CF catalyst in 0.5 M H_2SO_4 at 60 °C with sweep rate 20 mV s^{-1}.

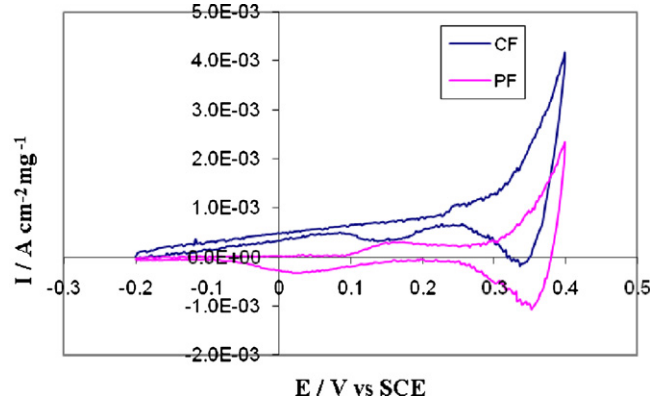

Fig. 15. CV of PF and CF up to 0.4 V in 0.5 M H_2SO_4 at 60 °C with sweep rate 20 mV s^{-1}.

4. Conclusion

Catalysed porous silver electrodes were prepared by two catalyst-loading strategies, postfired and cofired. The PF electrode possessed a catalyst particle size of 5.6 nm and was composed primarily of Pt–Ru alloy with a small amount of Ru. The PF catalyzed cathode surface was composed of mainly Ag with and a small amount of Pt–Ag alloy and exhibited little porosity due to pore blockage.

The CF catalyzed anode surface was composed of Pt–Ru alloy and precipitated Ru. The degree of alloy formation was greater for the CF anode catalyst than that of the PF catalyst. A bi-modal microstructure was obtained in the cofired anode catalyst in the form of precipitated whiskers composed mainly of Ag, Pt–Ru alloy with a small amount of Ru and the silver alloy matrix. The CF catalyzed cathode exhibited two morphologies: individual precipitated Pt particles and agglomerated Pt–Ag alloy. CV analyses revealed that the MOR on the CF catalyst was superior to that of PF catalyzed surface due to its higher surface area, uniform catalyst composition, higher degree of alloying and the contribution of a ternary catalytic effect. An evaluation of the performance of ORR under cathodic conditions for CF and PF catalysts revealed that ORR on the CF catalyzed cathode was superior to that of PF catalyst. Thus, it can be concluded that the CF method is the preferred route for preparing a catalyzed electrode for LTCC-based DMFCs.

References

[1] K. Kordesch, G. Simader, Fuel Cells and their Applications, 1st ed., Wiley–VCH, Weinheim, 1996.
[2] J. Pavio, J. Bostaph, A. Fisher, J. Hallmark, B.-J. Mylan, C. Xie, Microelectronics 29 (2002) 1–8.
[3] G.Q. Lu, C.Y. Wang, J. Power Sources 144 (2005) 141–145.
[4] R.G. Hockaday, M. DeJohn, C. Navas, P.S. Turner, H.L. Vaz, L.L. Vazul, Proceedings of the Fuel Cell Seminar, Portland, Oregon, USA, October 30 to November 2, 2000, p. 791.
[5] S. Tasic, D. Gervasio, R. Koripella, S.P. Rogers, S. Samms, J. Hallmark, Fuel Cell Seminar, Palm Springs, November 18–21, 2002, pp. 725–728.
[6] B.C.H. Steel, A. Heinzel, Nature 414 (2001) 345–352.
[7] D. Wilcox, R.F. Huang, S.X. Dai, Ceram. Trans. 97 (1999) 201–213.
[8] J.-H. Jean, Y.-C. Fang, S.X. Dai, D.L. Wilcox Sr., J. Am. Ceram. Soc. 84 (2001) 1354–1360.
[9] P. Wang, W.K. Jones, Y. Liu, Proceedings of the 2001 International Microelectronics Conference, IMAPS, Baltimore, MD, 2001.
[10] E. Antolini, F. Cardellini, J. Alloys Compd. 315 (2001) 118–122.
[11] J.W. Guo, T.S. Zhao, J. Prabhuram, R. Chen, C.W. Wong, Electrochim. Acta 51 (2005) 754–763.
[12] X. Xue, T. Lu, C. Liu, W. Xing, Chem. Commun. 12 (2005) 1601–1603.
[13] T. Kim, M. Takahashi, M. Nagai, K. Kobayashi, Electrochim. Acta 50 (2004) 813–817.
[14] L. Xiong, A. Manthiram, Solid State Ionics 176 (2005) 385–392.
[15] S. Rojas, F.J. Garcia, S. Jaras, M.V. Huerta, J.L.F. Fierro, M. Boutonnet, Appl. Catal. A: Gen. 285 (2005) 24–35.
[16] K. Lasch, L. Jörissen, J. Garche, J. Power Sources 84 (1999) 225–230.
[17] Z. Jusys, J. Kaiser, R. Behm, J. Electrochim. Acta 47 (2002) 3693–3706.
[18] Y. Lin, X. Cui, C.H. Yen, C.M. Wai, Langmuir 21 (2005) 11474–11479.
[19] S.L. Gojkovic, T.R. Vidakovic, D.R. Durovic, Electrochim. Acta 48 (2003) 3607–3614.
[20] V. Radmilovic, H.A. Gasteiger, P.N. Ross, J. Catal. 154 (1995) 98–106.
[21] B. Yang, Q. Lu, Y. Wang, L. Zhang, J. Lu, P. Liu, J. Wang, R. Wang, Chem. Mater. 15 (2003) 3552–3557.
[22] T.B. Massalski, Binary Alloys Phase Diagram, vol. 3, 2nd ed., ASM International, OH, 1990.
[23] L.P.R. Profeti, F.C. Simões, P. Olivi, K.B. Kokoh, C. Coutanceau, J.-M. Léger, C. Lamy, J. Power Source 158 (2006) 1195–1201.
[24] E.P. Grishina, E.M. Rumyantsev, Russ. J. Electrochem. 37 (2001) 474–478.
[25] E. Reddington, A. Sapienza, B. Gurau, R. Viswanathan, S. Sarangapani, E.S. Smotkin, T.E. Mallouk, Science 280 (1998) 1735.
[26] D.R. Venkataraman, H.R. Kunz, J.M. Fenton, J. Electrochem. Soc. 150 (2003) A278–A284.
[27] A.B. Anderson, E. Grantscharova, S. Seong, J. Electrochem. Soc. 143 (1996) 2075–2082.
[28] A. Lima, C. Coutanceau, J.-M. Léger, C. Lamy, J. Appl. Electrochem. 31 (2001) 379–386.
[29] X. Xue, J. Ge, C. Liu, W. Xing, T. Lu, Electrochem. Commun. 8 (2006) 1280–1286.
[30] T. Kawaguchi, Y. Rachi, W. Sugimoto, Y. Murakami, Y. Takasu, J. Appl. Electrochem. 36 (2006) 1117–1125.

[31] B. Gurau, R. Viswanathan, R. Liu, T.J. Lafrenz, K.L. Ley, E.S. Smotkin, E. Reddington, A. Sapienza, B.C. Chan, T.E. Mallouk, S. Sarangapani, J. Phys. Chem. B 102 (1998) 9997–10003.
[32] S. Mukerjee, J. McBreen, J. Electrochem. Soc. 146 (2006) 600–606.
[33] J. Perez, E.R. Gonzalez, E.A. Ticianelli, Electrochim. Acta 44 (1998) 1329–1339.
[34] D.A.J. Rand, R. Woods, Electroanal. Chem. Interfac. Electrochem 35 (1972) 209–218.
[35] T. Toda, H. Igarashi, H. Uchida, M. Watanabe, J. Electrochem. Soc. 146 (1999) 3750–3756.
[36] A.S. Arico, A.K. Shukla, H. Kim, S. Park, M. Min, V. Antonucci, Appl. Surf. Sci. 172 (2001) 33–40.
[37] A.K. Shukla, M. Neergat, P. Bera, V. Stamenkovic, P.N. Ross, Fuel Cells 1 (2001) 105–115.